Strontium Leaching Precedes $SrIrO_3$ Dissolution During Electrochemical Water Oxidation

Andrew R. Akbashev,[1,2,5]* Vladimir Roddatis,[3] Christoph Baeumer,[1,2,4] Tianchi Liu,[1] J. Tyler Mefford,[1,2] William C. Chueh[1,2]

[1]Department of Materials Science and Engineering, Stanford University, Stanford, CA 94305, USA.
[2]Stanford Institute for Materials and Energy Sciences, SLAC National Accelerator Laboratory, Menlo Park, CA, USA.
[3]German Research Centre for Geosciences GFZ, Helmholtz Centre Potsdam, Germany.
[4]Institute of Electronic Materials (IWE2) and JARA-FIT, RWTH Aachen University, Aachen, Germany.
[5]Present address: Division for Research with Neutrons and Muons, Paul Scherrer Institute, Villigen, Switzerland

* Corresponding authors: andrei.akbasheu@psi.ch

Mechanistic studies of oxide electrocatalysts for heterogeneous water oxidation have been primarily focused on understanding the origins of activity.[1,2] Despite encouraging progress, achieving long-term stability remains an important goal for their industrial implementation.[3–6] In this work, we study the degradation pathways of a highly active $SrIrO_3$ electrocatalyst during the oxygen evolution reaction (OER). $SrIrO_3$ serves as a model system for perovskite AMO_3 oxides as it can exhibit both A-cation leaching and transition metal (TM) oxide dissolution.[7–10] Employing epitaxial $SrIrO_3$ thin films, we explore the electrolyte- and potential-dependent leaching of Sr from the perovskite structure by following these processes through *operando* electrochemical atomic force microscopy (EC-AFM). Dissolution was imaged and quantified at the nanometer scale. We show that Sr leaching results in the *in-situ* formation of $Sr_{1-x}IrO_y$ layer, with the leaching rate controlled via electrolyte composition. Crucially, Sr leaching occurs at a potential > 0.5V lower than that for transition metal oxide dissolution. Our study demonstrates that suppression of the A-site leaching is crucial for improving the overall stability of perovskite oxide during electrocatalysis.

Oxygen evolution on transition metal (TM) oxides requires applied anodic potentials beyond their thermodynamic stability limits. These electrode materials can become structurally unstable and experience dissolution (corrosion) or form a passivating oxide layer. Both processes are strongly pH-dependent.[11] While known for their chemical tunability and a high OER activity, late TM oxides are prone to degradation during electrochemical water oxidation due to the formation of oxidized and water-soluble TM oxide species on the surface.[7,8,12–17] Several major pathways for the electrochemical degradation of an oxide electrocatalyst have been proposed. First, selective leaching of alkali and alkali-earth metals during the OER on oxide surfaces is ubiquitous. Under oxidative conditions, the formation of sub-stoichiometric surface layers results in structural transformations[12,13]. Second, oxidative dissolution of TMs from oxide surfaces is often observed at high overpotentials[5,16,18,19]. The rate of anodic dissolution of transition metals strongly depends on the chemical composition[4,16,20,29,30], structure[20,31] and crystallographic orientation[19] (facet) of a solid. Finally, the evolution of lattice oxygen can modify the ligand coordination of surface TM ions and lead to structural degradation.[21–23] For clarity, we define leaching as the deintercalation process that preserves the structural motif (topochemical reaction), while dissolution is a complete structural disintegration through the solvation process.

Strontium iridate ($SrIrO_3$), in particular, has recently attracted attention owing to its exceptionally high OER activity and susceptibility to Sr leaching and surface amorphization,[7–10,12,16,24–26] especially during the OER reaction in acidic electrolytes[8,9,25]. Electrochemical leaching of Sr^{2+} involves two holes ($h^{\bullet}$). The reaction in the Kröger-Vink notation is given below (see also Equations S1):

$$Sr_{Sr}^{\times} + Ir_{Ir}^{\times} + 2h^{\bullet} \longrightarrow V_{Sr}'' + Ir_{Ir}^{\bullet\bullet} + Sr_{solv.}^{\bullet\bullet} \quad \textbf{(Eq. 1)}$$

This reaction forms a surface layer of $Sr_{1-x}IrO_3$ containing a nominal Ir(VI). Previous studies showed that such Sr leaching can lead to the formation of an OER-active defect-rich and rough IrO_x surface layer[7,8]. This amorphization process was suggested to occur only during OER while being triggered by the lattice oxygen oxidation.[25]

Additional reactions may follow. One possibility is that the Sr-deficient layer evolves lattice oxygen via a partial Schottky reaction that restores Ir(IV) within the near-surface layer:

$$Ir_{Ir}^{\bullet\bullet} + O_O^{\times} + 2[OH]_{solv}' \longrightarrow Ir_{Ir}^{\times} + O_{2(g)} + H_2O \quad \textbf{(Eq. 2)}$$

Another possibility is that $Ir_{Ir}^{\bullet\bullet}$ can dissolve chemically (i.e., no net electron transferred):

$$Ir_{Ir}^{\bullet\bullet} + O_O^{\times} + 4[OH]_{solv}' \longrightarrow [IrO_4]_{solv}'' + 2H_2O \quad \textbf{(Eq. 3)}$$

Although several scenarios have been proposed[6,29,30,35], this mechanism involving the dissolution of Ir(VI) oxide seems to be most probable at high potentials because it is volatile and soluble in water[36,37]. We also note that this scenario can lead to the growth of amorphous and possibly hydrated IrO_x on the surface via a precipitation reaction[16]. Anodic dissolution of iridium during OER was observed for both metallic iridium[4,29,32–34] and Ir-containing oxides such as hydrous/amorphous[3,20,34] and rutile IrO_2 (ref. [3,4,20,32]), perovskite $SrIrO_3$,[20] double-perovskite Sr_2CoIrO_6 [16] and Ba_2PrIrO_6 [20].

While Sr leaching and iridium dissolution have been investigated separately, the relationship between the two processes is poorly characterized. In this work, we employ $SrIrO_3$ as a model system to understand the oxidative electrochemical behavior of perovskite electrocatalysts with complex chemistry and competing degradation pathways. Specifically, we study the structural and chemical evolution of single-crystalline $SrIrO_3$ surfaces during OER and its dependence on the electrolyte composition and pH.

Experimental results

To prepare a single-crystalline surface for the precise studies of its chemical and morphological evolution, we deposited $SrIrO_3$ epitaxial thin films on Nb-doped (001) $SrTiO_3$ substrates by pulsed laser deposition. Our electrodes were grown in a layer-by-layer mode and demonstrate high crystalline quality and step terraces on the surface (**Figure S1**), with thicknesses ranging from 10 to 120 nm. To quantify film thickness, we employed $Sr_3Al_2O_6$ liftoff pattern prior to $SrIrO_3$ deposition, creating a sharp step between the film and the substrate (**Figure S3**).

We first performed electrochemical experiments that involve cyclic voltammetry in 0.1M KOH (pH = 12.8) and 0.5M H_2SO_4 (pH = 0.29) electrolytes followed by *ex situ* AFM to

characterize the surface morphology (**Figure 1**). In KOH, $SrIrO_3$ dissolution initiates at the onset of OER, as evidenced by the decrease in film thickness (**Figure S7**). We observed that the step terraces remain topographically preserved, and electrochemical dissolution does not follow a step retreat[38,39] or etch pits formation[40] which are prevalent during chemical dissolution of crystals. Instead, the film dissolves uniformly, with step terraces remaining topographically visible even after a height loss of 10 nm (**Figure 1c-g, S6** and **S7**) and the roughness increasing with the amount of dissolved film (**Figure 1b**). In H_2SO_4, on the other hand, no dissolution is observed under these potentials. Instead, we observe ultrathin islands appearing at ~1.17 V *vs* RHE (Reversible Hydrogen Electrode) and disappearing after 1.5-1.6 V (**Figure 1h-l**). These islands, which we discuss below, noticeably impact the surface roughness (**Figure 1b**) but do not change the overall step-terraced morphology. We note that some islands were observed in KOH as well but there were significantly sparser than in H_2SO_4.

To gain further insights into the dissolution kinetics, we performed *operando* EC-AFM experiments, where the tip scans slowly along the edge between the exposed substrate and $SrIrO_3$ electrode during linear sweep voltammetry (LSV). Each fast line perpendicular to the edge generates a profile of the film with respect to the substrate (**Figure S3b**). Thus, we acquire a potential-dependent topography and thickness of $SrIrO_3$ in real time. Operando EC-AFM performed in KOH shows that, as the potential reaches 1.3-1.4 V, the $SrIrO_3$ surface develops ultrathin islands that extend tens of nm laterally and only few nm in thickness (**Figure 2a-b, S9**). These islands are immobile when scanned with an AFM tip and disappear as $SrIrO_3$ starts to dissolve at ~2 V (**Figure 2a, S9, S11, S12**). We speculate that these islands are $SrCO_3$ layers that appear following the reaction between leached Sr^{2+} and dissolved CO_3^{2-}. The CO_3^{2-} species are dominant at high pH[41] and originate from the dissolved CO_2 in the electrolyte that is exposed to air. At pH = 12.8, the Sr^{2+} concentration in equilibrium with $SrCO_3$ is only 23μM. In principle, one may expect a chemical precipitation[43,44] of $IrO_x{\cdot}nH_2O$ at high pH from the hydrolyzed species of Ir(III) or Ir(IV) (such as $[Ir(OH)_5(H_2O)]^{2-}$ or $[Ir(OH)_6]^{2-}$). However, we do not see such islands at higher potentials when the concentration of anodically dissolved iridium reaches the highest value in the solution.

In H_2SO_4, the behavior of $SrIrO_3$ is markedly different. **Figure 2d** shows the evolution of the topography, thickness and current density during a slow LSV sweep measured *in situ* with EC-AFM. The islands already appear at open-circuit and remain there until ~1.45 V (**Figure 2e**). The disappearance of the island occurs at a potential significantly lower than in the case of KOH (~1.9 V). These results are consistent with *ex situ* AFM imaging (**Figure 1h-l**). Importantly, for both slow LSV and CV sweeping (**Figure 2d, S10**), island formation occurs well below the OER onset, in contrast to the case of KOH, where the two potentials are very close. We propose that the islands are $SrSO_4$ ($K_{sp}(SrSO_4) = 2.33\times10^{-7}$)[45], with the equilibrium concentration Sr^{2+} being 24μM.

Next, we turn our attention to the evolution of the electrode thickness. The potential-dependent dissolution rates in both alkaline and acidic electrolytes extracted from the AFM data are plotted in **Figure 2g**. The onset potential of dissolution in KOH is ~1.9-2.0 V, with the rates reaching ~ 0.2 Å/s at 2.3 V. In H_2SO_4 the onset potential is substantially higher at 2.4 V with a rate of ~0.2 Å/s.

Using X-ray photoelectron spectroscopy (XPS), we characterized the Sr:Ir molar ratio at the surface (mean escape depth, MED, is 11.9 Å for Sr and 12.4 Å for Ir, see Methods) and subsurface (MED is 22.9 Å for Sr and 23.9 Å for Ir) regions after each 5-min potentiostatic hold, spanning both the pre-catalytic region and OER. Specifically, we found that strontium leaching in KOH proceeds from 1.3 to 1.5 V, at which point it levels off and remains constant (**Figure 2h**).

This decrease of the Sr:Ir molar ratio correlates well potential-wise with the appearance of ultrathin islands on the surface, consistent with our hypothesis that Sr^{2+} reacts with CO_3^{2-} to form $SrCO_3$. In H_2SO_4, Sr leaching is also observed but it does not level off with potential (**Figure 2h**), with over 70% of the "surface" Sr missing at the onset of dissolution at 2.3 V, which is substantially greater than in KOH. Importantly, when comparing **Figure 2g** and Figure **2h**, we can see significant potential gap (~ 0.6 V) between Sr leaching and active $SrIrO_3$ dissolution. The electrodes were also characterized by scanning transmission electron microscopy (STEM). The inset in **Figure 2h** shows STEM images (in the high-angle annular dark-field, HAADF) and the distribution of Sr and Ir obtained by mapping of electron energy loss spectra (EELS) in the film after the last measurement in H_2SO_4 shown in **Figure 2h**. The images reveal a highly disordered strontium-deficient $Sr_{1-x}IrO_3$ layer (~3-4 nm thick) on top of $SrIrO_3$. These results directly correlate with the XPS data. Similar layers were observed previously for $SrIrO_3$ tested in $HClO_4$ [25] and H_2SO_4 [7–9].

To understand the process during (bulk) dissolution, we perform *operando* EC-AFM galvanostatically at 10 mA/cm^2 in both alkaline and acidic electrolytes. In KOH, the film dissolution rate measured directly via *operando* EC-AFM is ~0.1 Å/s and remains constant with thickness (**Figure 3a**). Islands similar to those observed in slow LSV appear immediately once the potential is reached (**Figure S13 and S14**). The potential required to drive such high currents in the AFM liquid cell is higher than the potential measured in the RDE experiments due to a larger stagnant layer near the electrode surface inside the AFM cell than in the RDE cell. In H_2SO_4, on the other hand, EC-AFM shows no detectable dissolution of the 18-nm thick film over a period of 80 min (**Figure 3b, S15**), indicating a much higher stability at 10 mA/cm^2 than in the case of the basic electrolyte.

Next, we measure nominally identical $SrIrO_3$ electrodes (30 nm thick) galvanostatically at 10 mA/cm^2 in a rotating disk electrode (RDE) configuration. Because only a small fraction of the current is associated with the dissolution (as found in EC-AFM experiments), the potential measured in such galvanostatic experiments corresponds to the OER activity of the structurally evolving surface. **Figure 3c** shows the potential evolution in different electrolytes. $SrIrO_3$ in KOH shows a short 60-min plateau at ~1.8 V after which the potential increases rapidly, indicating a complete dissolution of the film as the potential exceeds 3 V. When a film dissolves completely in an RDE experiment, the dissolution time (until the potential starts to raise rapidly to 3 V) can be used to evaluate an average dissolution rate under galvanostatic conditions. The average dissolution rate in 0.1M KOH is 0.08 Å/s, consistent with the AFM results. For STEM studies, we characterized a 120-nm thick electrode after 60 mins at 10 mA/cm^2. STEM shows that the electrode does not have a noticeable Sr-depleted region (**Figure 3d**), in contrast to the results in acidic electrolytes. In 0.5M H_2SO_4 the film shows two plateaus: one at ~1.67 V with a longer stability than in the basic electrolyte and, importantly, the second plateau at ~2.32 V that continues for ~500 min while the potential increases slowly by ~120 mV. The estimation gives ~0.006 Å/s in 0.5M H_2SO_4 (consistent with EC-AFM), which is an order of magnitude smaller than in 0.1M KOH and correlates well with a negligible dissolution rate reported for IrO_2 in acids[4,22,32].

Discussion

In alkaline electrolyte, crossing the OER onset makes the surface Sr:Ir ratio drop below 0.75 (**Figure 1f**), while the subsurface ratio remains close to the stoichiometric value, indicating that Sr leaching in 0.1M KOH happens only within the first few unit cells of the surface. We suggest that the reason for such an exceptionally shallow leaching in the alkaline electrolyte

(unlike the "deep" leaching observed in acids and discussed below) is the rapid dissolution of the Sr-deficient ($Sr_{1-x}IrO_{3-y}$) surface layer after its formation, resulting in "chemical refreshing" of the surface. Such a stepwise dissolution of $SrIrO_3 \rightarrow Sr_{1-x}IrO_{3-y} \rightarrow SrIrO_3$ may be responsible for the preservation of the step terraces observed in EC-AFM experiments (Figure 1c-g) because the Ir-enriched surface is only transient in this process. This hypothesis is based on the Pourbaix diagrams of Ir-water system[11,33], where the anodic potential that corresponds to soluble iridium oxide species is noticeably lower at higher pH. Our conclusions are also supported by the previously reported density functional theory calculations on the thermodynamic surface stability of $SrIrO_3$.[37] In particular, Sr-depleted surface was found to be more stable than other surface compositions under thermodynamic potentials that correspond to OER conditions in our experiments, which implies that $Sr_{1-x}IrO_3$ is likely the surface layer that forms and later proceeds to the anodic dissolution. However, as such calculations do not consider solvation and are purely thermodynamic in nature, they cannot address the kinetics (rate) of the perovskite dissolution. As our study shows that $Sr_{1-x}IrO_3$ dissolves in actual experiments, we speculate that the mechanism for active dissolution involves the formation of highly oxidized iridium species at the surface (e.g., Ir(VI)) and follows Eq. 3. Importantly, in 0.5M H_2SO_4 (**Figure 3a, S10**) both Sr leaching and the islands appear at potentials that are earlier than the OER onset. These results do not support the mechanism proposed by Wan *et al*[25], where Sr leaching is initiated by the lattice oxygen oxidation reaction in the OER region. In our experiments, Sr leaching by itself does not lead to the perovskite dissolution. As **Figure 2d** shows, there is a wide potential gap (almost 0.6 V) between the onset of Sr leaching and active $SrIrO_3$ dissolution.

Next, we discuss the longer-term degradation behavior of the electrodes during galvanostatic measurements (10 mA/cm^2) in the RDE experiments (**Figure 3c**). In KOH, the dissolution follows a smooth potential curve. As the dissolution reaches completion, the potential rises rapidly to 3 V. The degradation of $SrIrO_3$ in H_2SO_4 is more complex. The EC-AFM experiments show a negligible dissolution rate at 10 mA/cm^2 (**Figure 3b**) and the Sr-depleted surface appears at OER potentials within a 5-min potentiostatic hold (**Figure 2h**). Based on these observations, we hypothesize that the two plateaus measured in 0.5M H_2SO_4 (**Figure 3c**, red curve) are related to two different states of the surface. The first low-potential plateau shows the activity of $Sr_{1-x}IrO_y$, while the high-potential plateau corresponds to the OER activity of a less active surface $IrO_y{\cdot}nH_2O$ layer. The transition between the two plateaus is determined by the interplay between the rates of Sr leaching and IrO_y dissolution. When Sr leaching is faster, it leads to the formation of a relatively stable Sr-depleted $IrO_y{\cdot}nH_2O$ layer. On the other hand, if Sr leaching is comparable or slower than $IrO_y{\cdot}nH_2O$ dissolution, then passivation does not take place and $SrIrO_3$ dissolves continuously. A very long high-potential plateau in H_2SO_4 implies that the anodic dissolution of $IrO_y{\cdot}nH_2O$ is significantly suppressed in H_2SO_4. Interestingly, previous studies reported different effects of prolonged testing of $SrIrO_3$ in acidic electrolytes on its OER activity. Specifically, in one study[7] $SrIrO_3$ films showed a small increase (2-fold) of activity during the first ~60 cyclic voltammetry sweeps but soon afterwards became much less active, without any change in the Tafel slope. On the contrary, in a different study[25] a moderate and continuous increase in activity (4-fold) was reported for $SrIrO_3$ films during 20-h cycling up to 1.75 V without any noticeable dissolution of the film. Finally, Seitz *et al.*[8] showed that $SrIrO_3$ films increase their activity almost 8-fold in 0.5M H_2SO_4 during galvanostatic measurements at 10 mA/cm^2. In our study, we do not see activity improvement during both prolonged cycling and galvanostatic tests (**Figure S5** and **S16**). While the reasons for such drastically different behavior of $SrIrO_3$ in the

aforementioned studies is unknown, it could be connected with a high sensitivity of the surface chemical composition and structure to the oxide film preparation conditions.

Because strontium leaching precedes an active dissolution stage by 0.5-1 V depending on the pH, we propose that Sr leaching is a necessary step in $SrIrO_3$ dissolution, which "prepares" the surface for easier oxidation and solvation by creating surface defects. To test this hypothesis, we attempt to suppress the Sr leaching by reducing its chemical potential difference between the $SrIrO_3$ and in the electrolyte. To do so, we use a 0.05M $Sr(OH)_2$ electrolyte which has Sr^{2+} concentration close to the saturation point and the same pH as that of 0.1M KOH. In XPS studies of the electrode after a 5-min potential hold in (**Figure S17**), we see a decreased amount of leached Sr at the surface compared to the electrode measured in both 0.1M KOH and 0.5M H_2SO_4 electrolytes. When the electrode is tested for much longer under harsher conditions (1-h galvanostatic hold at 10 mA/cm^2), a Sr-depleted layer at the surface of $SrIrO_3$ still appears (STEM-EELS, **Figure 4f**) similarly to the case of 0.5M H_2SO_4. Importantly, we note that while Sr leaching and $SrIrO_3$ dissolution occur at different potential, the galvanostatic experiments were performed at a starting potential of 2 V, and hence both processes occur concurrently. The galvanostatic test of the film in the 0.05M solution of $Sr(OH)_2$ (pH = 12.3) reveals a 2-3 times longer low-potential plateau that scales with the film thickness (**Figure 3c** and **S16**). Thus, because Sr-based electrolyte can extend the lifetime of $SrIrO_3$ in alkaline environment by decreasing the amount of leached Sr, we conclude that Sr leaching is the essential step in $SrIrO_3$ dissolution in alkaline electrolytes. In other words, Sr deficiency in the surface region promote an earlier onset of iridium dissolution.

In summary, we use *in situ* EC-AFM to characterize surface and thickness evolution of epitaxial $SrIrO_3$ thin-film electrocatalysts. Using this technique, we reveal the potential-dependent dissolution rate with a sub-nanometer precision within a large range of potentials extending deep into the OER region. Our study illustrates the complexity of the pH-dependent interplay between the IrO_y dissolution kinetics and Sr leaching during OER at the $SrIrO_3$ surface. Furthermore, we demonstrate that strontium leaching is an essential step during degradation of $SrIrO_3$ in an alkaline environment that promotes an earlier onset of iridium dissolution. Finally, we show that strontium leaching can be inhibited by using a $Sr(OH)_2$-based electrolyte, leading to a longer lifetime of the iridate electrocatalyst. Our work offers a new perspective on the means of studying the kinetics of oxide degradation and its mechanisms for electrocatalysts.

References

1. Hwang, J. *et al.* Perovskites in catalysis and electrocatalysis. *Science* **358**, 751 (2017).
2. Seh, Z. W. *et al.* Combining theory and experiment in electrocatalysis: Insights into materials design. *Science* **355**, (2017).
3. Danilovic, N. *et al.* Activity–Stability Trends for the Oxygen Evolution Reaction on Monometallic Oxides in Acidic Environments. *J. Phys. Chem. Lett.* **5**, 2474–2478 (2014).
4. Cherevko, S. *et al.* Oxygen and hydrogen evolution reactions on Ru, RuO_2, Ir, and IrO_2 thin film electrodes in acidic and alkaline electrolytes: A comparative study on activity and stability. *Catal. Today* **262**, 170–180 (2016).
5. Cherevko, S. Stability and dissolution of electrocatalysts: Building the bridge between model and "real world" systems. *Curr. Opin. Electrochem.* **8**, 118–125 (2018).

6. Spöri, C., Kwan, J. T. H., Bonakdarpour, A., Wilkinson, D. P. & Strasser, P. The Stability Challenges of Oxygen Evolving Catalysts: Towards a Common Fundamental Understanding and Mitigation of Catalyst Degradation. *Angew. Chem. Int. Ed.* **56**, 5994–6021 (2017).
7. Song, C. W., Suh, H., Bak, J., Bae, H. B. & Chung, S.-Y. Dissolution-Induced Surface Roughening and Oxygen Evolution Electrocatalysis of Alkaline-Earth Iridates in Acid. *Chem* **5**, 3243–3259 (2019).
8. Seitz, L. C. *et al.* A highly active and stable $IrO_x/SrIrO_3$ catalyst for the oxygen evolution reaction. *Science* **353**, 1011 (2016).
9. Lee, K., Osada, M., Hwang, H. Y. & Hikita, Y. Oxygen Evolution Reaction Activity in IrOx/SrIrO3 Catalysts: Correlations between Structural Parameters and the Catalytic Activity. *J. Phys. Chem. Lett.* **10**, 1516–1522 (2019).
10. Yang, L. *et al.* Efficient oxygen evolution electrocatalysis in acid by a perovskite with face-sharing IrO_6 octahedral dimers. *Nat. Commun.* **9**, 5236 (2018).
11. Pourbaix, M. *Atlas of Electrochemical Equilibria in Aqueous Solutions*. (National Association of Corrosion Engineers, 1966).
12. May, K. J. *et al.* Influence of Oxygen Evolution during Water Oxidation on the Surface of Perovskite Oxide Catalysts. *J. Phys. Chem. Lett.* **3**, 3264–3270 (2012).
13. Fabbri, E. *et al.* Dynamic surface self-reconstruction is the key of highly active perovskite nano-electrocatalysts for water splitting. *Nat. Mater.* **16**, 925 (2017).
14. Chang, S. H. *et al.* Functional links between stability and reactivity of strontium ruthenate single crystals during oxygen evolution. *Nat. Commun.* **5**, 4191 (2014).
15. Akbashev, A. R. *et al.* Activation of ultrathin $SrTiO_3$ with subsurface $SrRuO_3$ for the oxygen evolution reaction. *Energy Environ. Sci.* **11**, 1762–1769 (2018).
16. Zhang, R. *et al.* A Dissolution/Precipitation Equilibrium on the Surface of Iridium-Based Perovskites Controls Their Activity as Oxygen Evolution Reaction Catalysts in Acidic Media. *Angew. Chem. Int. Ed.* **58**, 4571–4575 (2019).
17. Zhang, R. *et al.* Importance of Water Structure and Catalyst–Electrolyte Interface on the Design of Water Splitting Catalysts. *Chem. Mater.* **31**, 8248–8259 (2019).
18. Rabe, M. *et al.* Alkaline manganese electrochemistry studied by in situ and operando spectroscopic methods – metal dissolution, oxide formation and oxygen evolution. *Phys Chem Chem Phys* **21**, 10457–10469 (2019).
19. Roy, C. *et al.* Trends in Activity and Dissolution on RuO2 under Oxygen Evolution Conditions: Particles versus Well-Defined Extended Surfaces. *ACS Energy Lett.* **3**, 2045–2051 (2018).
20. Geiger, S. *et al.* The stability number as a metric for electrocatalyst stability benchmarking. *Nat. Catal.* **1**, 508–515 (2018).
21. Grimaud, A. *et al.* Activation of surface oxygen sites on an iridium-based model catalyst for the oxygen evolution reaction. *Nat. Energy* **2**, 16189 (2016).
22. Kasian, O. *et al.* Degradation of iridium oxides via oxygen evolution from the lattice: correlating atomic scale structure with reaction mechanisms. *Energy Env. Sci* **12**, 3548–3555 (2019).
23. Zagalskaya, A. & Alexandrov, V. Role of Defects in the Interplay between Adsorbate Evolving and Lattice Oxygen Mechanisms of the Oxygen Evolution Reaction in RuO2 and IrO2. *ACS Catal.* **10**, 3650–3657 (2020).
24. Kuo, D.-Y. *et al.* Influence of Strain on the Surface–Oxygen Interaction and the Oxygen Evolution Reaction of $SrIrO_3$. *J. Phys. Chem. C* **122**, 4359–4364 (2018).

25. Wan, G. *et al.* Amorphization mechanism of $SrIrO_3$ electrocatalyst: How oxygen redox initiates ionic diffusion and structural reorganization. *Sci. Adv.* **7**, eabc7323 (2021).
26. Chen, Y. *et al.* Exceptionally active iridium evolved from a pseudo-cubic perovskite for oxygen evolution in acid. *Nat. Commun.* **10**, 572 (2019).
27. Chen, Y. *et al.* Exceptionally active iridium evolved from a pseudo-cubic perovskite for oxygen evolution in acid. *Nat. Commun.* **10**, 572 (2019).
28. Scholz, F. & Kahlert, H. *Chemical Equilibria in Analytical Chemistry: The Theory of Acid–Base, Complex, Precipitation and Redox Equilibria*. (2019). doi:10.1007/978-3-030-17180-3.
29. Cherevko, S., Geiger, S., Kasian, O., Mingers, A. & Mayrhofer, K. J. J. Oxygen evolution activity and stability of iridium in acidic media. Part 1. – Metallic iridium. *J. Electroanal. Chem.* **773**, 69–78 (2016).
30. Cherevko, S., Geiger, S., Kasian, O., Mingers, A. & Mayrhofer, K. J. J. Oxygen evolution activity and stability of iridium in acidic media. Part 2. – Electrochemically grown hydrous iridium oxide. *J. Electroanal. Chem.* **774**, 102–110 (2016).
31. Geiger, S. *et al.* Activity and Stability of Electrochemically and Thermally Treated Iridium for the Oxygen Evolution Reaction. *J. Electrochem. Soc.* **163**, F3132–F3138 (2016).
32. Kasian, O., Grote, J.-P., Geiger, S., Cherevko, S. & Mayrhofer, K. J. J. The Common Intermediates of Oxygen Evolution and Dissolution Reactions during Water Electrolysis on Iridium. *Angew. Chem. Int. Ed.* **57**, 2488–2491 (2018).
33. Schalenbach, M. *et al.* The Electrochemical Dissolution of Noble Metals in Alkaline Media. *Electrocatalysis* **9**, 153–161 (2018).
34. Jovanovič, P. *et al.* Electrochemical Dissolution of Iridium and Iridium Oxide Particles in Acidic Media: Transmission Electron Microscopy, Electrochemical Flow Cell Coupled to Inductively Coupled Plasma Mass Spectrometry, and X-ray Absorption Spectroscopy Study. *J. Am. Chem. Soc.* **139**, 12837–12846 (2017).
35. Binninger, T. *et al.* Thermodynamic explanation of the universal correlation between oxygen evolution activity and corrosion of oxide catalysts. *Sci. Rep.* **5**, 12167 (2015).
36. Pourbaix, M. J. N., Van Muylder, J. & De Zoubov, N. Electrochemical properties of the platinum metals. *Platin. Met. Rev.* **3**, 47–53 (1959).
37. Raman, A. S., Patel, R. & Vojvodic, A. Surface stability of perovskite oxides under OER operating conditions: A first principles approach. *Faraday Discuss* **229**, 75–88 (2021).
38. Kuwahara, Y. In situ Atomic Force Microscopy study of dissolution of the barite (001) surface in water at 30°C. *Geochim. Cosmochim. Acta* **75**, 41–51 (2011).
39. Miyata, K. *et al.* Dissolution Processes at Step Edges of Calcite in Water Investigated by High-Speed Frequency Modulation Atomic Force Microscopy and Simulation. *Nano Lett.* **17**, 4083–4089 (2017).
40. Noiriel, C., Oursin, M., Saldi, G. & Haberthür, D. Direct Determination of Dissolution Rates at Crystal Surfaces Using 3D X-ray Microtomography. *ACS Earth Space Chem.* **3**, 100–108 (2019).
41. Andersen, C. B. Understanding Carbonate Equilibria by Measuring Alkalinity in Experimental and Natural Systems. *J. Geosci. Educ.* **50**, 389–403 (2002).
42. Högfeldt, E. *Stability Constants of Metal-Ion Complexes: Part A. Inorganic Ligands*. (Pergamon, 1984).
43. Zhao, Y., Vargas-Barbosa, N. M., Hernandez-Pagan, E. A. & Mallouk, T. E. Anodic Deposition of Colloidal Iridium Oxide Thin Films from Hexahydroxyiridate(IV) Solutions. *Small* **7**, 2087–2093 (2011).

44. Zhao, Y. *et al.* Understanding the Effect of Monomeric Iridium(III/IV) Aquo Complexes on the Photoelectrochemistry of $IrO_x \cdot nH_2O$-Catalyzed Water-Splitting Systems. *J. Am. Chem. Soc.* **137**, 8749–8757 (2015).
45. Reardon, E. J. & Armstrong, D. K. Celestite (SrSO4(s)) solubility in water, seawater and NaCl solution. *Geochim. Cosmochim. Acta* **51**, 63–72 (1987).
46. Marshall, W. L. & Jones, E. V. Second Dissociation Constant of Sulfuric Acid from 25 to 350° Evaluated from Solubilities of Calcium Sulfate in Sulfuric Acid Solutions1,2. *J. Phys. Chem.* **70**, 4028–4040 (1966).
47. Powell, C. J. Practical guide for inelastic mean free paths, effective attenuation lengths, mean escape depths, and information depths in x-ray photoelectron spectroscopy. *J. Vac. Sci. Technol. A* **38**, 023209 (2020).
48. Tanuma, S., Powell, C. J. & Penn, D. R. Calculations of electron inelastic mean free paths. V. Data for 14 organic compounds over the 50–2000 eV range. *Surf. Interface Anal.* **21**, 165–176 (1994).
49. Jablonski, A. & Powell, C. J. Practical expressions for the mean escape depth, the information depth, and the effective attenuation length in Auger-electron spectroscopy and x-ray photoelectron spectroscopy. *J. Vac. Sci. Technol. A* **27**, 253–261 (2009).
50. Chambers, S. A. & Du, Y. Experimental determination of electron attenuation lengths in complex materials by means of epitaxial film growth: Advantages and challenges. *J. Vac. Sci. Technol. A* **38**, 043409 (2020).

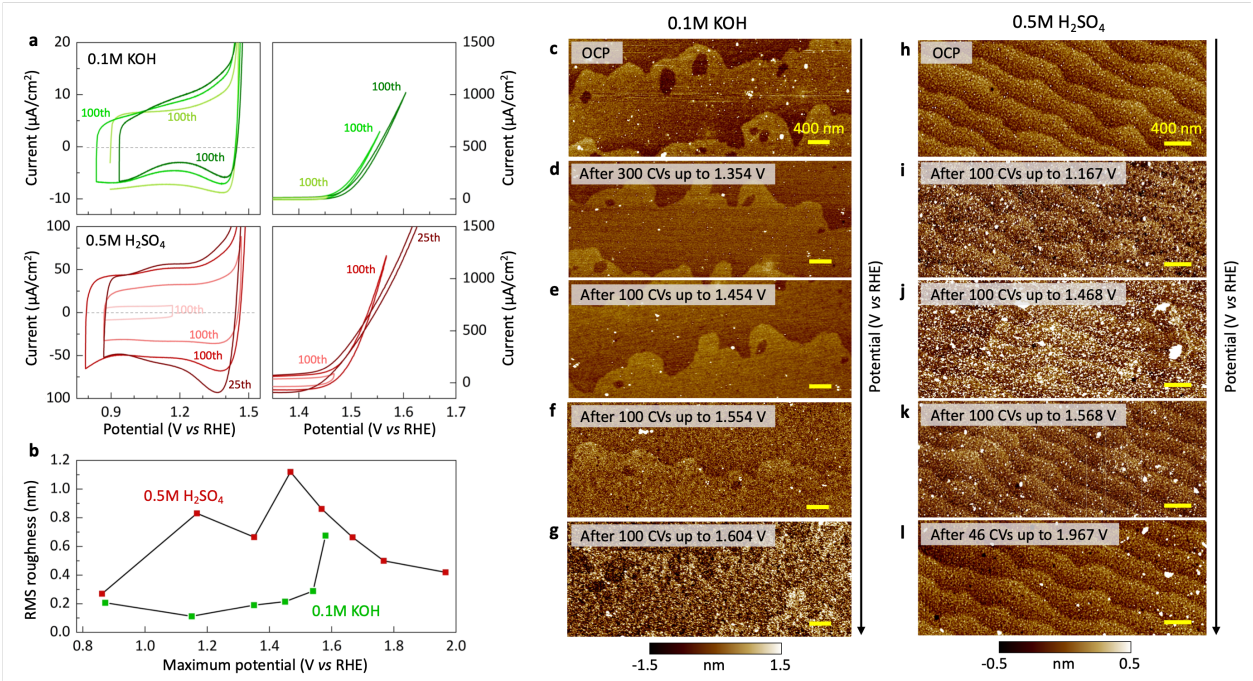

Figure 1. (a) Capacitive and OER regions of the $SrIrO_3$ film after a given number of cycles up to a given potential. (b) The room mean square (RMS) roughness after each CV series up to a maximum potential in 0.1M KOH and 0.5M H_2SO_4. (c-l) The surface roughening as the cycling is done to increasingly higher potentials in 0.1M KOH and 0.5M H_2SO_4, corresponding to CV conditions given in (a) and (b) (scale bars are 400 nm). See Figure S6 and S8 for further data and information.

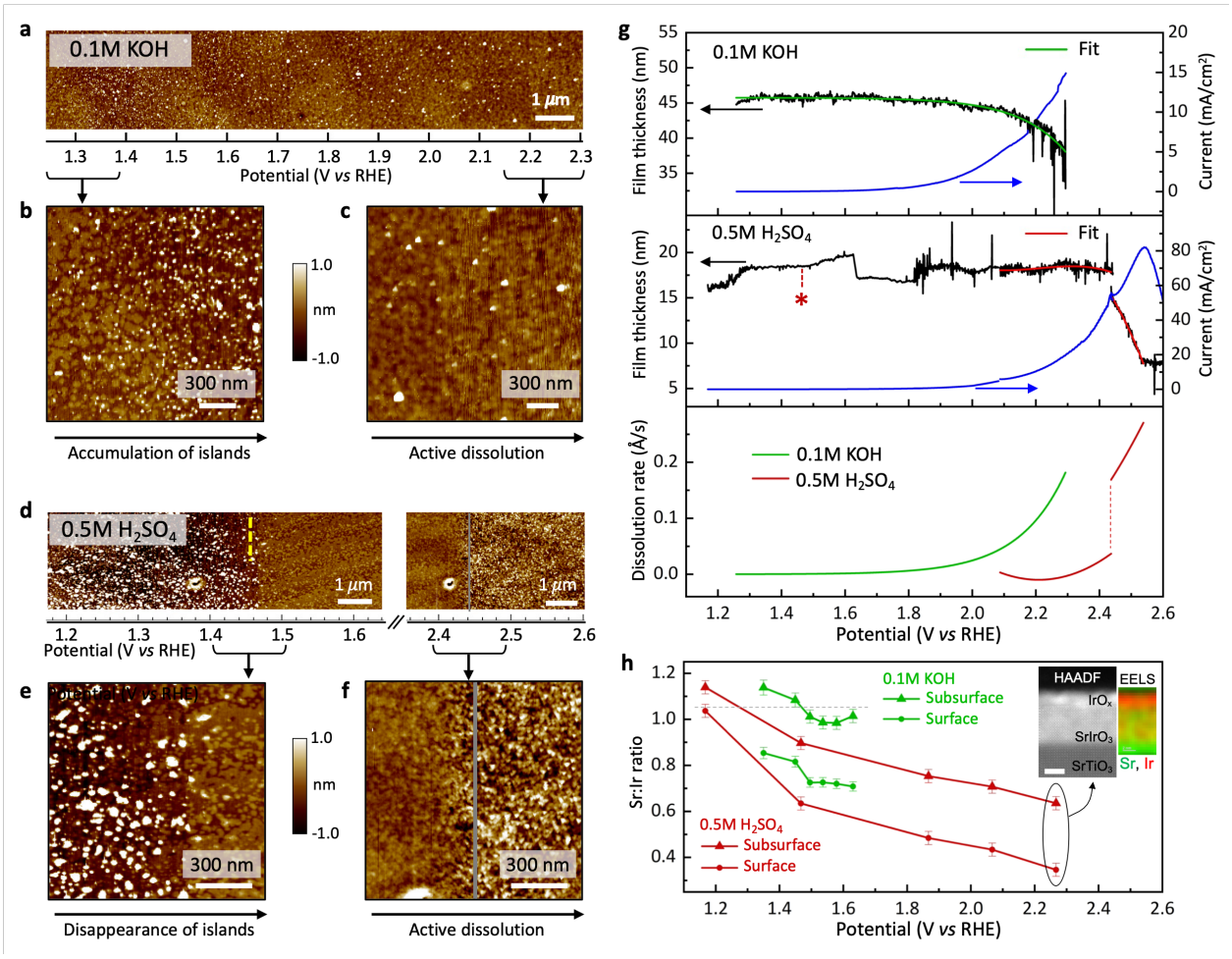

Figure 2. (a) Electrochemical *operando* EC-AFM measurements of the $SrIrO_3$ film in 0.1M KOH (see also Figure S9). (b) An enlarged region of the AFM image showing the initiation of the surface evolution with potential manifested in the appearance of islands on the surface without the loss of the step-terraced surface morphology. (c) Active dissolution phase (the image is flattened for clarify). (d) The evolution of the $SrIrO_3$ film in 0.5M H_2SO_4 (see also Figure S10). (e-f) Disappearance of islands from the surface and the beginning of active dissolution of $Sr_{1-x}IrO_3$. (g) Evolution of the film thickness in 0.1M KOH and 0.5M H_2SO_4 with potential obtained in the *operando* EC-AFM experiment. The dissolution rate is evaluated by fitting the thickness as a function of time (green curve – exponential fit, red curve – 3rd degree polynomial fit). The red asterisk marks the potential at which the islands on the surface in (d) disappear (yellow dashed line). (h) X-ray photoelectron spectroscopy showing Sr depletion at the surface near the OER onset potential for the two electrolytes. The error bars represent standard deviation in percentage (derived from the standard deviation of the five XPS measurements performed on an as-grown film). The inset shows the HAADF STEM image and EELS map of the film after the *ex situ* XPS measurements in 0.5M H_2SO_4 showing a heavily Sr-depleted surface $Sr_{1-x}IrO_y$ layer. The scale bar is 3nm.

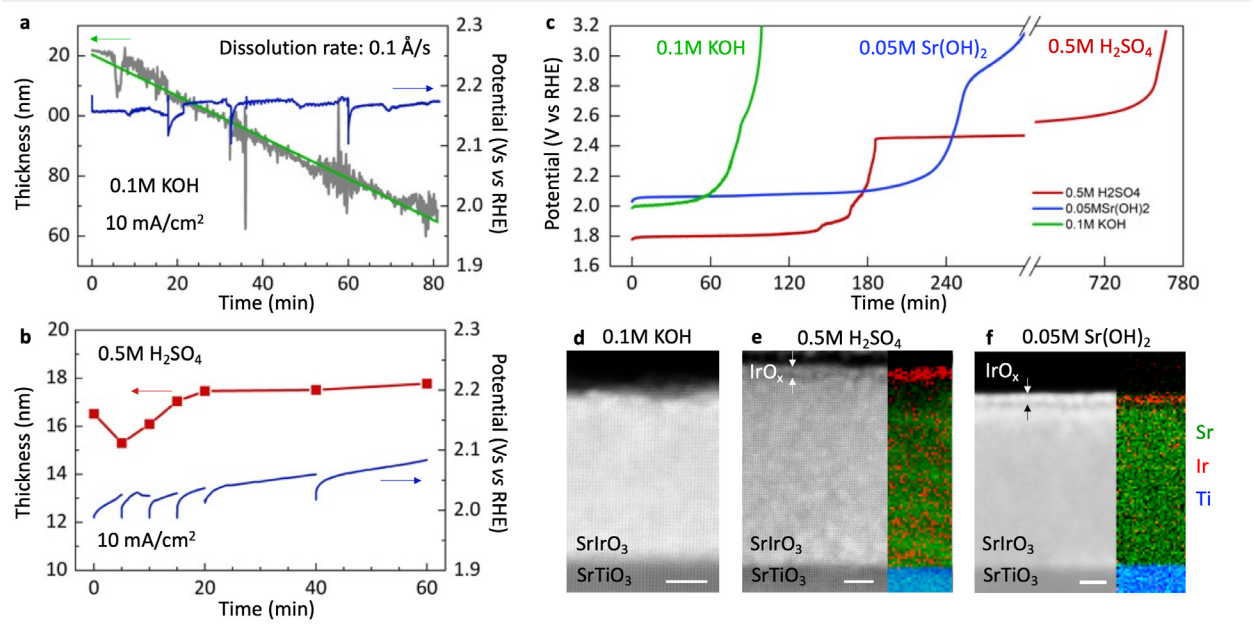

Figure 3. (a-b) Thickness variation of the $SrIrO_3$ film during galvanostatic measurements at 10 mA/cm² in 0.1M KOH and 0.5M H_2SO_4 obtained in *operando* EC-AFM experiments (see more data in Figure S13, S14, S15). (c) Evolution of potential in galvanostatic measurements (at 10 mA/cm²) in an RDE cell showing the variation of OER current as the films with identical thickness (30 nm) undergo anodic corrosion in different electrolytes. (d-f) HAADF images and EELS maps of the cross sections of the films tested galvanostatically at 10 mA/cm² for 1 h in different electrolytes. Colored EELS maps show Sr (green), Ir (red) and Ti (blue) elemental distribution. Because of the difference in dissolution rates in these electrolytes, the starting thickness of the films was not the same.

Methods

Thin film preparation and characterization

Thin films of $SrIrO_3$ were grown by pulsed laser deposition (PLD/MBE 2300, PVD Products) on 10x10 mm^2 (001) Nb-doped $SrTiO_3$ (0.5 wt% doping) (Shinkosha Co., Japan) using $SrIrO_3$ target (Toshima Manufacturing, Japan). All substrates were first etched with buffered HF solution (pH = 4.5) and annealed at 950 °C under Argon flow for 2 hours to restore high-quality step terraces. The growth temperature was 700 °C under oxygen pressure of 30 mTorr (some samples were grown under 15 mTorr). The target to substrate distance was 84 mm, the laser fluence was 2 J/cm^2. The growth was monitored *in situ* using a RHEED system (TorrRHEEDt, Staib Instruments) operated at 35 kV (1.5 mA). The samples with the $SrIrO_3$-$SrTiO_3$ step were prepared through the following steps: (i) a small area on the substrate was covered with acetone-soluble photoresist (Megaposit SPR3612); (ii) an amorphous layer (20-30nm) of water-soluble $Sr_3Al_2O_6$ was grown at room temperature in the PLD from the $Sr_3Al_2O_6$ in-house prepared target; (iii) the photoresist was then removed using acetone, leaving a clean area on the substrate; (iv) $SrIrO_3$ layer was grown on top of the entire sample under conditions mentioned above; (v) finally, the sample was immersed in water for several hours and lightly sonicated to dissolve $Sr_3Al_2O_6$ and remove the $SrIrO_3$ layer grown above it but leaving the $SrIrO_3$ layer in the area previously protected by the photoresist. Such samples had a small area (0.1-0.3 mm^2) of the $SrIrO_3$ film on a large-area substrate and were used in the majority of electrochemical AFM experiments. X-ray diffraction and X-ray reflectivity of thicker films were collected using PANalytical X'Pert PRO diffractometer equipped with a double monochromator and operating in a parallel- beam geometry.

Transmission electron microscope specimens were prepared by focused ion beam lift-out technique using a Thermofisher Scientific Helios UC instrument operated at 30 kV at the beginning of preparation, followed by 5 and 2 kV for the final cleaning. The HAADF and EELS images were collected with a Thermofisher Scientific (former FEI) image-corrected Titan 80-300 environmental TEM operated at 300 kV, equipped with a Gatan Imaging Filter Quantum 965 ER. Another set of specimens were analyzed with a Thermofisher Scientific probe-corrected Themis Z microscope operated at 80 kV, and equipped with a Gatan Imaging Filter Continuum 1065 ER.

The air-free XPS characterization was performed with a PHI Versa Probe (Physical Electronics Inc.) with Al Kα X-ray illumination, a pass energy of 23.5 eV and at various photoemission angles without neutralization. The samples were measured in the RDE cell inside a nitrogen-filled glovebox and transferred to XPS in a transfer vessel without air exposure. The Sr:Ir stoichiometry was calculated using integrated intensity of the respective peaks after subtraction of the Shirley background (fitting was done with CasaXPS) and the sensitivity factors of 5.7772 (Sr) and 16.1333 (Ir). The mean escape depth was defined through the inelastic mean free path (IMFP) of the photoelectrons λ and the photoemission angle θ through $d = \lambda \times \cos\theta$.[47] IMFP was calculated to be 23.8 Å for Sr and 24.7 Å for Ir using QUASES-IMFP-TPP2M.[48] This isotropic approach uses the straight-line approximation[49], as is suitable in the absence of well-characterized, material-specific angle-dependent effective attenuation lengths. For a full description of the information depth in photoemission the readers are referred to the literature .

Electrochemical measurements

Electrochemical measurements of the thin films were performed using a rotating disk electrode (RDE, Pine Research) setup under 1000-1500 r.p.m. Teflon cell was used. Only the front

side of the film was exposed to the electrolyte (film area is 10x10mm^2, while the electrolyte-contacted area is circular with a diameter of 7.5 mm), and the potential was controlled using a BioLogic SP-300 potentiostat. On the electrolyte side, a film area of 0.75 mm diameter was exposed to the electrolyte and sealed using an O-ring (FFKM, Marco Rubber). Electrical contact was made from the back of the substrate, where the Ti(5 nm) and Pt(50-100 nm) layers were deposited beforehand. The O_2-saturated electrolyte solutions used in the experiments were prepared using the following chemicals: KOH pellets (Sigma-Aldrich, Semiconductor grade, 99.99%), concentrated H_2SO_4 (99.99 %), $Sr(OH)_2{\cdot}8H_2O$ (Alfa Aesar, 99%). A set of carefully maintained Hg/HgO reference electrodes (CHI152, CH Instruments) filled with 1M KOH were used in the experiments involving alkaline and neutral electrolytes, with a separate "master" electrode that was used for calibration purposes (typical deviations were within 1-3 mV). The 1M KOH electrolyte inside the Hg/HgO electrode was replaced after each measurement in the chemically non-native $Sr(OH)_2$ electrolyte. Similarly, Hg/Hg_2SO_4 reference electrodes (RREF0025, Pine Research) were used in the 0.5M H_2SO_4. We found that our heterostructures exhibit a solid-state film-substrate junction resistance that is potential-dependent. This makes an accurate correction for resistance difficult. As a result, no correction for the resistance-induced potential drop was done for all samples (the data are as measured). The concentration of Sr^{2+} in equilibrium with $SrCO_3$ was calculated using the solubility constant K_{sp} ($SrCO_3$) = 5.6×10^{-10}.[42]

Electrochemical Atomic Force Microscopy

Atomic Force Microscopy was performed using Oxford Instruments Asylum Cypher ES scanning probe microscope and a modified liquid cell. The scans were recorded in a tapping mode using Olympus AC55TS tips (radius ~7 nm) that were excited photothermally (blueDriveTM) on the gold-coated reflex side. These tips can operate in liquid at high resonance frequency (~ 1 MHz, have a stable resonance and therefore are ideal for high-resolution imaging. In the scanning process, the phase was kept close to 70-80% to make sure the tip operated in a repulsive regime without a significant mechanical force. The Asylum software package implemented into Igor Pro was used for flattening and correcting the AFM images. When islands appeared on the surface, depending on the tip-sample interaction, the tip could go afloat. When such lines were occasional, they were removed from the scan using the "Erase line" function under "Modify Panel" in the Asylum software. When the lines were not occasional, they were left as is.

Electrochemical AFM experiments were done in the original liquid cell from Asylum Research but modified to incorporate all three electrodes, one of which was a real reference electrode (Hg/HgO for 0.1M KOH and Hg/Hg_2SO_4 for 0.5M H_2SO_4). During OER reaction inside the AFM cell, a continuous electrolyte flow was maintained using a combination of separate "push-pull" syringe pumps (PHD ULTRA, Harvard Apparatus) at a rate of 50-500 μL min^{-1} depending on the current.

Acknowledgements

A.R.A, C.B., J.T.M., and W.C.C. acknowledge funding provided by the U.S. Department of Energy (DOE), Office of Basic Energy Sciences, Division of Materials Sciences and Engineering (contract DE-AC0276SF00515). Part of this work was performed at the Stanford Nano Shared Facilities (SNSF)/Stanford Nano-fabrication Facility (SNF), supported by the National Science Foundation under award ECCS-1542152. V.R. acknowledges the European Regional Development Fund and the State of Brandenburg for the Themis Z TEM (part of the Potsdam

Imaging and Spectral Analysis Facility (PISA)), and the use of equipment in the Collaborative Laboratory and User Facility for Electron Microscopy (CLUE) at University of Göttingen. The financial support by the Deutsche Forschungsgemeinschaft, grant number CRC 1073 (Projects Z02) is highly appreciated.

Author contributions

A.R.A, J.T.M. and W.C.C. conceived the idea. A.R.A designed the experiments, performed the deposition and characterization of the films, electrochemical RDE measurements, and *operando* EC-AFM. Tianchi Liu helped with additional film preparation and XRD. V.R. prepared TEM specimens and performed the electron microscopy. C.B. performed *ex situ* XPS. All authors contributed to the discussion of the results and writing of the manuscript.